PHOTONICS Research

Ultrafast carrier dynamics and nonlinear optical response of InAsP nanowires

Junting Liu,[1] He Yang,[2,4] Vladislav Khayrudinov,[3] Harri Lipsanen,[3] Hongkun Nie,[1,*] Kejian Yang,[1] Baitao Zhang,[1] and Jingliang He[1]

[1]State Key Laboratory of Crystal Materials, Institute of Novel Semiconductors, Shandong University, Jinan 250100, China
[2]Summa Semiconductor Oy, Micronova, Espoo FI-00076, Finland
[3]Department of Electronics and Nanoengineering, Aalto University, Espoo FI-00076, Finland
[4]e-mail: yhyanghe@gmail.com
*Corresponding author: hknie@sdu.edu.cn

Received 27 April 2021; revised 4 July 2021; accepted 6 July 2021; posted 6 July 2021 (Doc. ID 430172); published 24 August 2021

Indium arsenide phosphide (InAsP) nanowires (NWs), a member of the III–V semiconductor family, have been used in various photonic and optoelectronic applications thanks to their unique electrical and optical properties such as high carrier mobility and adjustable band gap. In this work, we synthesize InAsP NWs and further explore their nonlinear optical properties. The ultrafast carrier dynamics and nonlinear optical response are thoroughly studied based on the nondegenerate pump probe and Z-scan experimental measurements. Two different characteristic carrier lifetimes (~2 and ~15 ps) from InAsP NWs are observed during the excited-carrier relaxation process. Based on the physical model analysis, the relaxation process can be ascribed to the carrier cooling process via carrier-phonon scattering and Auger recombination. In addition, based on the measured excited-carrier lifetime and Pauli-blocking principle, we discover that InAsP NWs show strong saturable absorption properties at the wavelengths of 532 and 1064 nm. Last, we demonstrate for the first time a femtosecond (~426 fs) solid-state laser based on an InAsP NWs saturable absorber at 1.04 μm. We believe that our work provides a better understanding of the InAsP NWs optical properties and will further advance their photonic applications in the near-infrared range.

https://doi.org/10.1364/PRJ.430172

1. INTRODUCTION

In the past two decades, nanowires (NWs) have been employed as versatile building blocks [1–3] used in various optoelectrical devices [4–7] because of their tailored optical and electronic properties [8,9]. Semiconductor NWs exhibit many unique physical characteristics such as significant surface and size effects [10], building blocks for nanoelectronics [7], and Majorana fermions [11]. For example, the electrical and optical properties of semiconductor NWs can be tuned by controlling their sizes, shapes, and compositions [12,13]. For instance, alloyed III–V semiconductor ternary $GaAs/In_xGa_{1-x}As$ nanowires show continuous tuning of the bandgap (0.91–1.52 eV) by adjusting the ratio of In and Ga elements [12]. In addition, the bandgap of semiconductor NWs decreases with increasing size [13]. Thus, semiconductor NWs are useful and multifunctional nanomaterials working as various building blocks to advance the research of photonic and optoelectronic devices, such as solar cells [1,14], lasers [2,15], and photodetectors [3,16].

Owing to the large electron g-factor and small electron effective mass [17–19], III–V semiconductor NWs have been applied in nanoscale optoelectronic devices [17], infrared detectors [18], and spin electronics [19]. Known as the representative of the III–V semiconductor family, InAsP NWs which were first synthesized by Pettersson in 2006 [3] show great potential for infrared photodetectors due to the high carrier mobility. Since then, great efforts have been devoted to pursuing InAsP NW-based optoelectronic devices, such as high-speed electronics [20,21] and near-infrared light emitters and detectors [22–24]. In theory, the bandgap of InAsP NWs can be tailored from 0.35 to 1.35 eV by adjusting the alloy composition, covering the important telecommunication wavelength band from 1.3 to 1.55 μm [25]. Besides, the growth of InAsP NWs has larger tolerance for lattice mismatch than thin-film epitaxial growth, which allows adjusting the optical nonlinear sensitivity through external bending or twisting strain [26,27] and has more flexibility in substrate selection and mechanical properties. Thus, there is a demand to study the intrinsic optical properties (e.g., carrier dynamics, nonlinear optical absorption) of InAsP NWs in the near-infrared wavelength range, which remains unexplored.

In this work, we fabricate high-quality InAsP NWs by directly growing them on a quartz substrate using the Au

nanoparticle-assisted vapor-liquid-solid (VLS) method. Then, the carrier dynamics of InAsP NWs is investigated by nondegenerate pump-probe measurements, which show that the excited carrier in InAsP NWs exhibits one fast (~2 ps) and one slow (~15 ps) relaxation processes. Furthermore, we study the nonlinear absorption properties of InAsP NWs by tuning the light intensity and wavelength using the Z-scan technique. We find that InAsP NWs have a large nonlinear absorption coefficient ($\beta_{\text{eff}} \sim 10^2$ cm/MW) and positive nonlinear refractive index ($n_2 \sim 10^{-13}$ m^2/W), which is much higher than the reported values of other nanomaterials including graphene, transition metal dichalcogenides (TMDs), and black phosphorus (BP). The studies on the ultrafast carrier relaxation dynamics and nonlinear optical absorption properties show the potential of InAsP NWs in the application field of optical switching. By using InAsP NWs as a saturable absorber (SA), a passively mode-locked laser at 1.04 μm is demonstrated with the shortest pulse width of 426 fs. Our results prove that InAsP NWs could be very promising candidates as excellent nonlinear optical modulators used in photonic and electronic devices.

2. RESULTS AND DISCUSSION

A. Preparation and Characterization of InAsP NWs

InAsP NWs samples are grown on quartz substrates inside a horizontal flow atmospheric pressure metal-organic vapor phase epitaxy (MOVPE) system. The detailed process can be found in Appendix A.1. Scanning electron microscopy (SEM) is used to examine the surface morphology of the prepared NWs. Figure 1(a) depicts the as-grown InAsP NWs that have an average diameter of ~50 nm with smooth surfaces (shown in the inset). Atomic force microscopy (AFM) image together with the height profile provides further evidence for the uniform formation of InAsP NWs. As shown in Figs. 1(b) and 1(c), the diameter of InAsP NWs is determined to be ~50 nm (average value), which is consistent with Au particle diameter. What is more, we did the energy-dispersive X-ray spectroscopy (EDX) along the growth direction to study the crystal structure of InAsP NWs, as shown in Fig. 1(d), which illustrates the high quality of our InAsP NWs sample solely consisting of In, As, and P without additional elements and the ratio of In, As, and P elements is about 2:2:1. Figure 1(e) shows the Raman spectrum of the InAsP NWs excited by a 532 nm laser with the power of 2 mW. The peaks observed at 217.6 and 247.8 cm^{-1} are InAs-like modes which correspond to a transverse optical (TO_1) and a longitudinal optical (LO_1) phonon modes. The peaks around 298.1 cm^{-1} are InP-like modes corresponding to a transverse optical phonon mode (TO_2), which is consistent with the previous research [28]. Photoluminescence (PL) measurement [Fig. 1(f)], performed at room temperature, reveals only one PL peak at 1280 nm, corresponding to the band-to-band transition in bulk form.

B. Ultrafast Carrier Dynamics of InAsP NWs

Pump-probe spectroscopy with femtosecond resolution is employed at room temperature to study the relaxation process of the excited carriers in InAsP NWs. A schematic of the experimental setup is shown in Fig. 2(a) (details in Appendix A.2). Pump light with wavelength of 400 nm is used to stimulate electrons from the ground state to the excited state, while the probing is done at the wavelength of 675 nm. It is worth noting that pump-probe spectroscopy is a nondestructive method, so no damage is induced to the samples. Figure 2(b) shows the photoinduced bleaching signal (positive $\Delta T/T$) under different pump energy intensities (from 47.7 to 197.4 $\mu\text{J}/\text{cm}^2$). The increase in the transmission right after excitation indicates the saturable absorption of the InAsP NWs due to

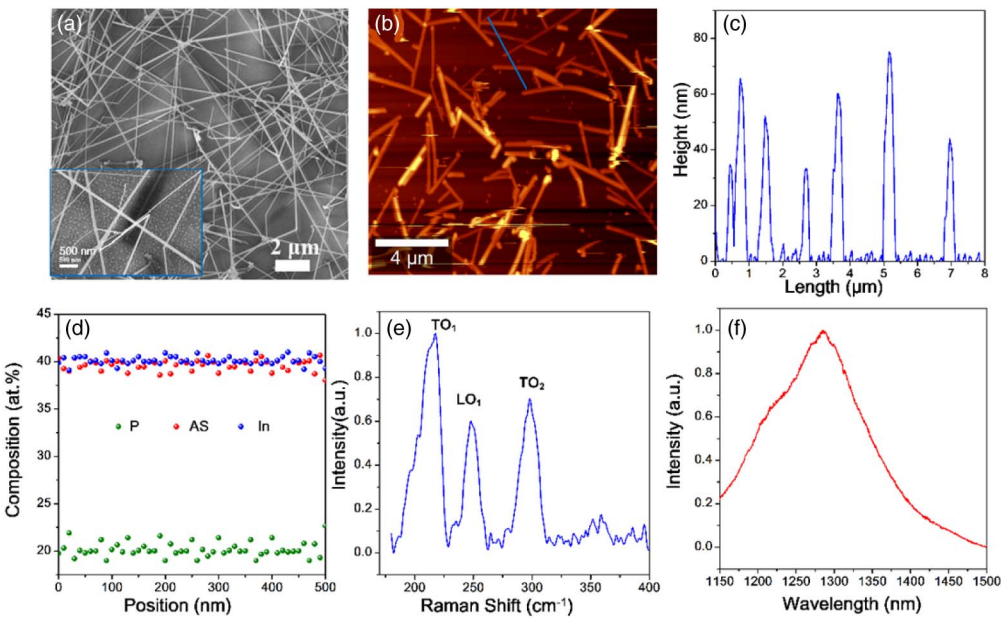

Fig. 1. (a) SEM image of InAsP NWs on quartz substrate. The inset is a higher-resolution SEM image, which shows the NW diameter of ~50 nm. (b) AFM image of InAsP NWs. (c) Height profiles along the line in the AFM image. (d) EDX measurement of InAsP NWs along the growth direction. (e) Raman spectrum measured using a 532 nm laser. (f) Room-temperature PL spectrum of InAsP NWs.

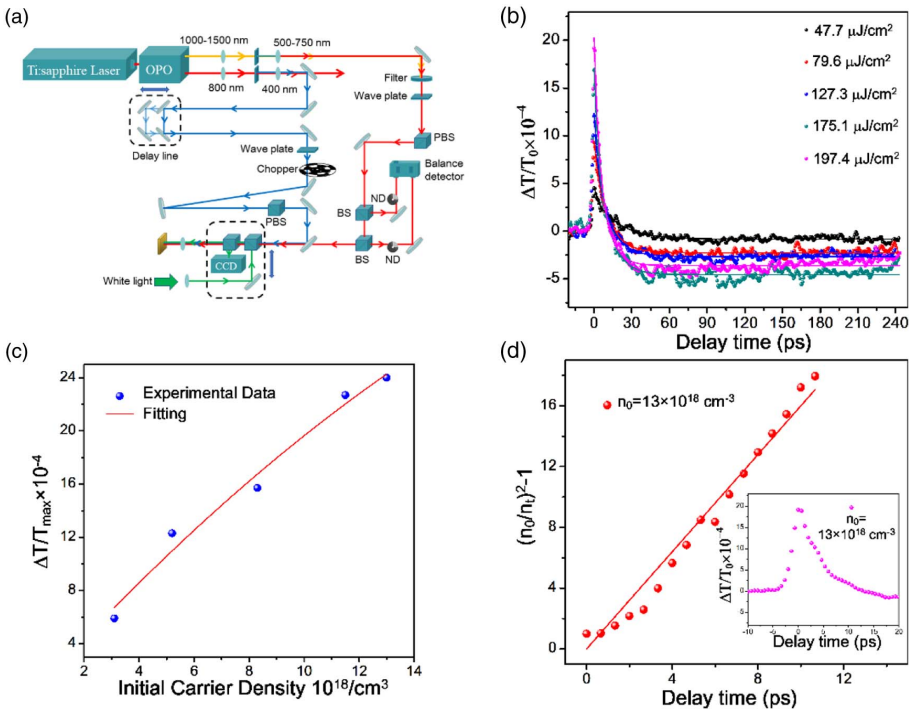

Fig. 2. (a) Experimental setup of the nondegenerate pump-probe measurement. (b) Differential transmission of InAsP NWs at different pump pulse energies with a 675 nm probe laser. (c) Relationship between maximum differential transmission and initial photoinduced carrier density. (d) Linear fit to $(n_0/n_t)^2 - 1$ as a function of pump-probe delay time and initial photoinduced carrier density.

the Pauli-blocking effect. To further analyze the carrier dynamics, we employ a biexponential decay model [29]:

$$\frac{\Delta T}{T_0}(t) = A_1 e^{-t/\tau_1} + A_2 e^{-t/\tau_2}, \tag{1}$$

where τ_1 and τ_2 ($\tau_1 < \tau_2$) represent the carrier lifetimes, and A_1 and A_2 are the corresponding relative amplitudes. Good fit to experimental data shown in Fig. 2(b) is obtained with Eq. (1), and the fitted parameters are listed in Table 1. Two clearly different characteristic carrier lifetimes τ_1 and τ_2 are identified. It is worth noting that their time scale is about two orders of magnitude larger than the duration of the pump light (~150 fs). The values of the short carrier lifetimes (τ_1) are ~2 ps, independent of the pump intensity. Such ultrafast relaxation time (in ps order) can be ascribed to the carrier cooling process via carrier-phonon scattering, which is consistent with the phenomenon observed in graphite [30]. At the same time, the slow time scale (~20 ps) decreases with the increase of the pump intensity, and the pump fluence dependence of the measured lifetimes is consistent with carrier capture by defects via Auger scatterings [31]. Because the defect-assisted Auger recombination is a three-particle effect in which carrier–carrier interactions become increasingly significant at high carrier densities; the lifetime is inversely proportional to the carrier concentration, and as the carrier concentration increases, the defect concentration is constant, so the proportion of this process is gradually decreasing.

Table 1. Fitted Parameters on the Carrier Relaxation Time of InAsP NWs from Eq. (1)

Pump Energy Intensity (μJ/cm²)	τ_1 (ps)	τ_2 (ps)	A_1	A_2
47.7	1.89 ± 0.93	19.27 ± 0.89	0.192	0.803
79.6	2.53 ± 1.65	11.17 ± 0.67	0.145	0.855
127.3	2.26 ± 0.65	10.79 ± 0.49	0.228	0.772
175.1	1.77 ± 0.59	10.12 ± 0.55	0.250	0.750
197.4	2.65 ± 1.20	7.95 ± 0.78	0.252	0.748

The photoinduced carrier dynamics relaxed from the excited states to the valence band is commonly described by a three-term rate equation [32–34]:

$$-\mathrm{d}n/\mathrm{d}t = \alpha n + \beta n^2 + \gamma n^3, \tag{2}$$

where t is the relaxation time, n is the excited carrier density, and α, β, and γ are the first, second, and third terms, respectively, which represent first-order Shockley-Read-Hall (SRH) recombination, free-carrier recombination, and Auger recombination. Figure 2(c) plots the maximum bleach signal measured as a function of the pump energy density, which is modeled by the phenomenological expression [35,36]

$$\left[\frac{\Delta T}{T}\right]_{\max} = \frac{A n_0}{B + n_0^C}, \tag{3}$$

where A, B, and C are fitting parameters. The initial charge carrier density (n_0) can be calculated by $n_0 = j\alpha_0$, where α_0 is the InAsP NWs absorption coefficient, and j is the pump fluence (photons per cm²). Therefore, we can correlate differential transmission $\Delta T/T$ to the density of photogenerated charge carriers using the above expression.

After converting the measured $\Delta T/T$ signal into photogenerated carrier density, the third-order rate equation can be obtained by eliminating the first- and second-order terms in Eq. (2) and assuming the numbers of photogenerated electrons and holes are equal, which can be expressed as follows:

$$\frac{n_0^2}{n_t^2} - 1 = kn_0^2 t, \tag{4}$$

where k is the third-order rate constant for the recombination process. By linear fitting of Eq. (4), we obtain the initial photoinduced carrier density (n_0) of 13×10^{18} cm^{-3}, as shown in Fig. 2(d). Then the Auger recombination rate of $(9.5 \pm 0.2) \times 10^{-27}$ cm^6 s^{-1} is obtained.

C. Nonlinear Optical Response of InAsP NWs

The open-aperture (OA) and closed-aperture (CA) Z-scan techniques are effective ways to investigate the nonlinear optical (NLO) responses of the InAsP NWs through the measurement of their nonlinear absorption and refraction. The details are given in Appendix A.3. The intensity-dependent normalized transmittance as a function of Z position at 532 and 1064 nm is shown in Figs. 3(a) and 3(c). For a certain incident laser energy, the transmittance curve is symmetrical at the focus point which has a Gaussian-like shape, arising from the saturation absorption of the InAsP NWs. To obtain the saturable absorption phenomena, various lenses with different focus lengths are used for the different excitation lasers. Typically, the normalized transmittance for InAsP NWs can be written as [37]

$$T(Z) = \sum_{n=0}^{\infty} (-\beta_{\text{eff}} I_0 L_{\text{eff}})^n \Big/ \left(1 + \frac{Z^2}{Z_0^2}\right)^n (n+1)^{3/2}$$
$$= 1 - \beta_{\text{eff}} I_0 L_{\text{eff}} / 2^{\frac{3}{2}} \left(1 + \frac{Z^2}{Z_0^2}\right), \tag{5}$$

where Z_0 and I_0 are the Rayleigh length and the peak on-axis intensity at the focus ($Z = 0$), respectively. L_{eff} and β_{eff} are the effective thickness and effective nonlinear absorption coefficient of the InAsP NWs, respectively. β_{eff} can be obtained by fitting the OA Z-scan measurement data with different incident pulse energies. The results show that β_{eff} is -207 ± 2.3 and -144 ± 0.7 cm/MW at 532 and 1064 nm, separately. It is worth noting that the value of β_{eff} remains constant for different incident energies, which indicates that the nonlinear absorption process of InAsP NWs is dominated by the single-photon saturable absorption. The values of β_{eff} are much larger than those of the most 2D materials such as graphene [38], transition metal dichalcogenides (TMDs) [38,39], black phosphorus (BP) [40], and MXenes [41], as shown in Table 2. In addition, it is also comparable to our previous results on InAs NWs [42], indicating a strong saturable absorption capability. The imaginary part of the third-order nonlinear optical susceptibility ($\text{Im}\chi^{(3)}$) can be calculated with the following formula [41]:

$$\text{Im}\chi^{(3)} = \frac{2\varepsilon_0 c^2 n_1^2}{3\omega} \beta_{\text{eff}}, \tag{6}$$

where ε_0 is the vacuum permeability, c is the vacuum light speed, ω is the angular frequency, and n_1 is the linear refractive index.

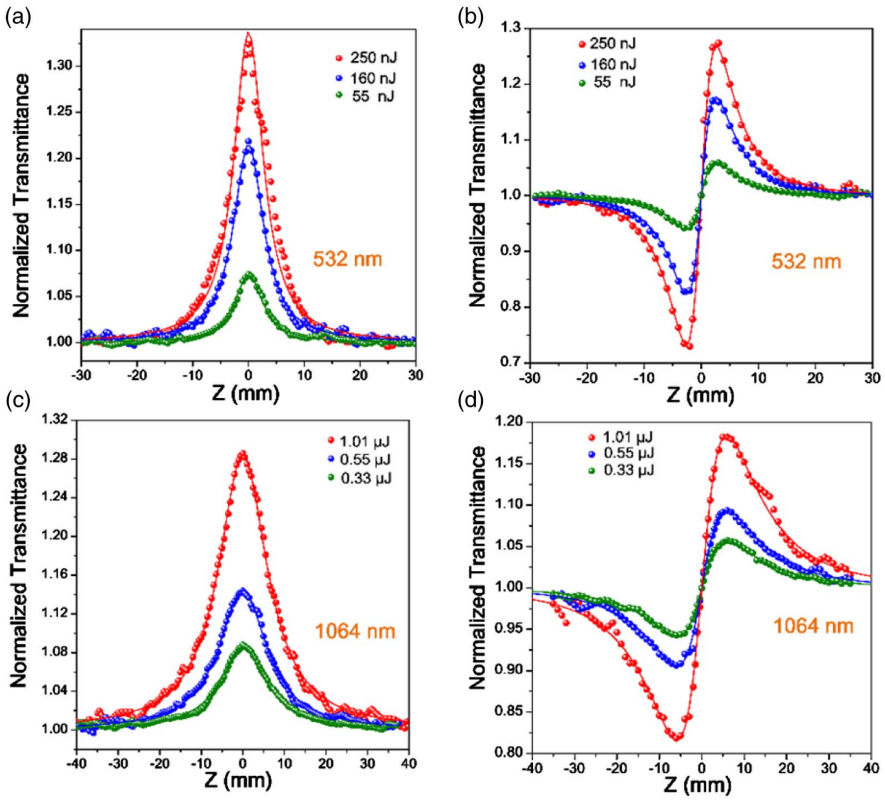

Fig. 3. Characterization of the NLO properties of the InAsP NWs. OA Z-scan measurements of the InAsP NWs at (a) 532 nm and (c) 1064 nm. CA Z-scan measurements of the InAsP NWs at (b) 532 nm and (d) 1064 nm.

Table 2. Comparison of β_{eff} and n_2 Values between InAsP NWs and Other Nanomaterials

Materials	Laser Parameters	β_{eff} (cm/GW)	n_2 (m^2/W)	Reference
Graphene	1030 nm, 1 kHz, 340 fs	$-(19.27 \pm 0.89) \times 10^{-2}$	-13.7×10^{-16}	[38]
MoS_2	532 nm, 10 kHz, 100 ps	-26.2 ± 8.8	$-(2.5 \pm 1.2) \times 10^{-16}$	[38]
WS_2	1064 nm, 20 Hz, 25 ps	-5.1 ± 0.26	$(5.83 \pm 0.18) \times 10^{-15}$	[39]
BP	800 nm, 10 kHz, 100 fs	-1.38×10^{-2}	—	[40]
MXene	800 nm, 1 kHz, 95 fs	-0.07	-3.47×10^{-20}	[41]
InAs NWs	1064 nm, 50 kHz, 100 ns	-1×10^{8}	—	[42]
InAsP NWs	532 nm, 200 kHz, 10 ps	$-(2.07 \pm 0.02) \times 10^{5}$	$(2.39 \pm 0.03) \times 10^{-13}$	This work
InAsP NWs	1064 nm, 200 kHz, 10 ps	$-(1.44 \pm 0.01) \times 10^{5}$	$(2.73 \pm 0.02) \times 10^{-13}$	This work

As shown in Appendix B (Table 3), the calculated $\text{Im}\chi^{(3)}$ shows a similar trend as β_{eff} with the values of $(-2.63 \pm 0.03) \times 10^{-7}$ and $(-3.7 \pm 0.02) \times 10^{-7}$ esu for 532 and 1064 nm, respectively. To further characterize the saturable absorption properties of InAsP NWs, the optical transmittance as a function of the incident laser intensity is fitted based on a two-level system (see Appendix C). The values of I_s and ΔR for different wavelengths are summarized in Table 3 by fitting the experimental data. The highest modulation depths are determined to be 33.7% ± 0.2% and 19.2% ± 0.2%, while the average saturation intensities I_s are 0.8 ± 0.02 and 0.25 ± 0.008 GW/cm^2 at 532 and 1064 nm, respectively. The saturation intensity is inversely proportional to the wavelength that is in agreement with the two-level energy system model ($I_s = h\nu/\sigma\tau_r$), where σ is the absorption cross section, $h\nu$ is the photon energy, and τ_r is the decay time. The observed saturation intensities of the InAsP NWs saturable absorber are lower than that based on graphene (170±51 GW/cm^2) [38], TMDs (114 ± 63 GW/cm^2) [38,39], BP (459 GW/cm^2) [40], and MXenes (69.3 GW/cm^2) [41], which is very promising for mode-locking process.

The CA Z-scan technique is used to characterize the refractive index (n_2) of the sample. The normalized transmittances of the closed aperture Z-scan results under different incident energies at the wavelength of 532 and 1064 nm are shown in Figs. 3(b) and 3(d). The normalized transmittance can be fitted using the following formula [43]:

$$T = 1 + \frac{4kL_{\text{eff}}n_2I_0Z}{Z_0(Z^2/Z_0^2 + 9)(Z^2/Z_0^2 + 1)}, \tag{7}$$

where $k = \frac{2\pi}{\lambda}$, and n_2 is the nonlinear refractive index. The valley–peak shapes of the normalized transmittance CA/OA Z-scan curves, which result from the Kerr effect induced self-focusing effect in InAsP NWs, suggest the positive refractive index. The obtained nonlinear refractive index is 2.39 ± 0.03 and $2.73 \pm 0.02 \times 10^{-13}$ m^2/W at 532 and 1064 nm. The real part of the third-order nonlinear optical susceptibility ($\text{Re}\chi^{(3)}$) can be expressed as [40]

$$\text{Re}\chi^{(3)} = \frac{4\varepsilon_0 c n_1^2}{3} n_2. \tag{8}$$

The $\text{Re}\chi^{(3)}$ is $(7.17 \pm 0.01) \times 10^{-7}$ esu (at 532 nm) and $(8.2 \pm 0.01) \times 10^{-7}$ esu (at 1064 nm). As listed in Table 2, n_2 of InAsP NWs is slightly higher than that of typical 2D materials, such as graphene [35], TMDs [35,36], and MXene [38].

D. Ultrafast Photonic Applications

Because InAsP NWs exhibit strong third-order nonlinear optical response and ultrafast saturation recovery time, it is meaningful to further explore their ability on the generation of ultrashort pulses. Here, a mode-locked solid-state laser based on InAsP NWs saturable absorber is assembled. Based on the mode-locking theory, when the mode-locking pulse energy is larger than the minimum intracavity pulse energy, the stable continuous-wave (CW) laser can be demonstrated. Therefore, considering the SA parameters, the following formula should be satisfied [41]:

$$F_{\text{sat},A}\Delta R < \frac{(PT_R)^2}{F_{\text{sat},L}A_{\text{eff},L}A_{\text{eff},A}} = \frac{(PT_R)^2 \times m\sigma_{\text{em},L}\lambda}{hc \times \pi\omega_{\text{eff},L}^2 \times \pi\omega_{\text{eff},A}^2}, \tag{9}$$

where P is the intracavity pulsed laser power, T_R is the round-trip time, and $F_{\text{sat},A}$ and $F_{\text{sat},L}$ are the saturation fluence of SA and laser gain medium, respectively. $A_{\text{eff},L}$ and $A_{\text{eff},A}$ are the effective laser mode on the laser gain medium and SA, respectively, h is the Planck constant, c is the light velocity, $\sigma_{\text{em},L}$ is the emission cross section of the laser crystal, $\omega_{\text{eff},L}$ and $\omega_{\text{eff},A}$ are the effective laser modes radii on the laser gain medium and SA, respectively, and m is a cavity constant: $m = 1$ for a ring cavity, and $m = 2$ for a linear cavity. Based on ABCD propagation matrix, a 3.5 m long Z-type resonator is designed. The setup details are given in Appendix A.4. Here, the $\omega_{\text{eff},L}$ and $\omega_{\text{eff},A}$ are calculated as 37 and 54 μm, respectively. The left-hand side of Eq. (9), $F_{\text{sat},A}\Delta R$, is calculated to be 2.5 μJ/cm^2, which is smaller than the right-hand side (11.2 μJ/cm^2). Therefore, based on the as-designed and the as-prepared InAsP NWs SA, stable CW mode-locked lasers can be obtained.

When the absorbed pump power exceeds 4.26 W, stable CW mode-locked (CWML) operation is established. Figure 4(a) depicts the relationship between the absorbed pump power and average output power. The obtained maximum average output power is 333 mW under the absorbed pump power of 7.17 W. Once the absorbed pump power exceeds 7.17 W, the CWML operation is broken. The output power instabilities (RMS) are measured to be less than 2% over 1 h. By sech^2 pulse shape fitting listed in Fig. 4(b), the pulse duration is measured to be 426 fs. The inset shows that the spectrum is centered at 1043 nm with a full-width-at-half-maximum (FWHM) of 3.1 nm, corresponding to the time-bandwidth product of 0.364, which is higher than the Fourier transform-limited value (0.315). It indicates that the output pulses are slightly chirped. Also, the radio-frequency spectra are recorded with different spans. As shown in Fig. 4(c), the fundamental peak is located at 42.93 MHz with

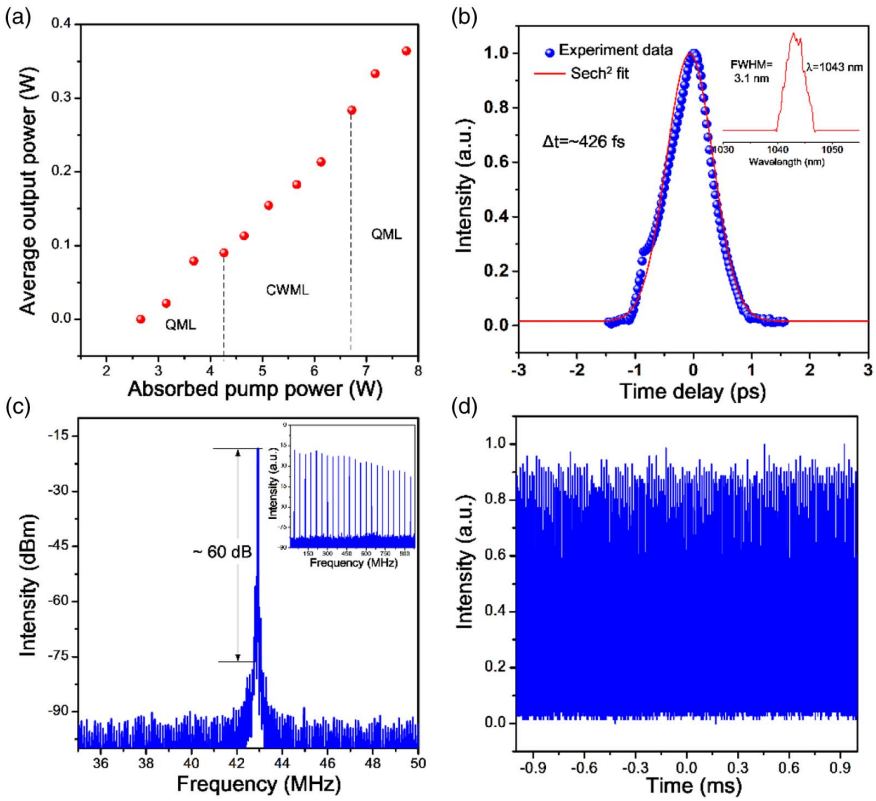

Fig. 4. Mode-locked laser results based on InAsP NWs. (a) Average output power versus absorbed pump power. (b) The measured pulse width by autocorrelation spectroscopy is ~426 fs. Inset: corresponding spectrum centered at 1043 nm. (c) Recorded frequency spectrum of the mode-locked laser with an RBW of 10 kHz. Inset: 1 GHz wide-span spectrum. (d) Recorded CWML pulse trains under the maximum pump power.

a signal-to-noise ratio of 60 dB. No spurious frequency modulations are observed in a wide span of 1 GHz with a resolution bandwidth (RBW) of 75 kHz, which proves clean CWML operation based on InAsP NWs. What is more, the CWML pulse trains show good amplitude stability with a time span of 2 ms [Fig. 4(d)]. The mode-locked laser based on InAsP NWs shows a relatively short pulse width and relatively high output power, which indicates the InAsP NWs are promising SA for the ultrafast laser generation.

3. CONCLUSIONS

In summary, we fabricate InAsP NWs by using an Au nanoparticle-assisted VLS growth method. The NLO properties and ultrafast carrier dynamics of InAsP NWs have been studied by Z-scan and nondegenerate pump-probe measurements for the first time. The excited carriers of InAsP NWs exhibit two characteristic carrier lifetimes (fast ~2 ps and slow ~15 ps), which can be attributed to a carrier cooling process via carrier-phonon scattering and an Auger recombination process. Besides, Z-scan measurements demonstrate that InAsP NWs have excellent NLO properties with a large nonlinear absorption coefficient of $\sim 10^2$ cm/MW and nonlinear refractive index of $\sim 10^{-13}$ m^2/W. Furthermore, we successfully demonstrate the femtosecond mode-locked solid-state laser based on InAsP NWs SA. Our work indicates that InAsP NWs are excellent candidates for applications in photonic and electronic devices.

APPENDIX A: EXPERIMENTAL METHODS

1. Growth of InAsP NWs

InAsP NWs were grown on quartz substrates inside a horizontal flow atmospheric pressure metal-organic vapor phase epitaxy (MOVPE) system using an Au nanoparticle–assisted vapor-liquid-solid (VLS) growth method. Trimethylindium (TMIn), tertiarybutylarsene (TBAs) and tertiarybutylphosphine (TBP) were used as precursors. First, the substrates were cleaned in an ultrasonic bath with isopropanol (IPA) and acetone, rinsed in deionized water, and then treated with a poly-L-lysine (PLL) solution for 120 s. Next, the surface was treated with 40 nm diameter colloidal gold (Au) nanoparticles solution (BBI International, UK) for 120 s. Prior to the growth, the substrates were annealed *in situ* at 600°C for 10 min under hydrogen flow to desorb surface contaminants. The NW growth temperature was fixed at 410°C for 5 min with the TMIn, TBAs, and TBP flows of 2.8, 14.4, and 1276 μmol/min, respectively. The nominal V/III ratio during the growth was ~460. After the growth, the TBP source kept on until the reactor cooled down to 250°C to protect the NW surface from desorption. Hydrogen was used as a carrier gas, and the total reactor gas flow rate was ~5 L/min. The growth temperatures reported in this work are thermocouple readings of the

lamp-heated graphite susceptor, which are slightly higher than the real substrate surface temperature. The structural analysis of the NWs was performed using scanning electron microscopy (SEM) (Zeiss Supra 40).

2. Nondegenerate Micro Pump-Probe Measurements

The setup was established using Ti:sapphire oscillators (800 nm, 80 MHz, 150 fs), separated to two components. One beam was used to drive the optical parametric oscillator to generate the pulses from 1000 to 1500 nm. After frequency doubling through a BBO crystal, the wavelength of the beam was changed to 500–750 nm. The wavelength of 650 nm was used as the probe light. The other beam was fixed at 400 nm and was used as the pump light. Both the pump and probe light were focused onto the sample by a 20× objective lens, and the pump fluence was 20 times higher than the probe fluence. The CCD camera (Thorlabs, DCC1545M) was used to image the sample and to check that the centers of pump and probe light coincide. The pump-induced change of the probe was detected by an adjustable gain balanced photoreceiver (Newport, 2317NF). The chopper frequency was fixed to 1 kHz as the reference frequency of the lock-in amplifier. The initial charge carrier density (n_0) can be calculated by the following formula:

$$n_0 = \frac{\lambda E a_0}{\omega_0^2 \pi h c}, \tag{A1}$$

where λ is the wavelength of excitation light, E is the pump energy fluence, ω_0 is the beast waist (~5 μm), h is the Planck constant, c is the speed of light in vacuum, and the absorption coefficient (a_0) of InAsP NWs is $\sim 1.02 \times 10^5\ \mathrm{cm}^{-1}$.

3. Z-scan Measurement

Z-scan measurements were performed using a homemade mode-locked Yb fiber laser (center wavelength 1064 nm, repetition rate 100 kHz–1 MHz, pulse duration 10 ps), which can generate a signal with the wavelength of 532 nm by doubling the frequency through a BBO crystal. The pulses were divided to two parts: one was set as a reference light, collected by a power meter (Thorlabs S470C); the other was focused by a lens into the samples. Lenses of different focusing lengths were used for different wavelength of incident light, $f = 50$ mm for 532 nm and $f = 75$ mm for 1064 nm, and the focused beam waist was estimated to be 26 and 52 μm. The sample was fixed to a stepper motor which was controlled by a computer program.

4. CW Mode-Locking Operation

We transferred the as-grown InAsP NWs grown on quartz onto a mirror with high-reflection (HR) coating at 1020–1100 nm via a PMMA-mediated method. Yb^{3+}-ion-doped (5%, atom fraction) Yb:KGW crystal (3 mm × 3 mm × 2 mm) was used as the gain medium. It was wrapped in indium foil and cooled by running water at a temperature of 18°C to accelerate thermal conduction. The pump source was a 27 W fiber-coupled laser diode (numerical aperture of 0.22, core diameter of 105 μm) emitting at 976 nm, which was focused into the laser gain medium via a 1.8:1 coupling optics system with a diameter of 58 μm and well matched with the diameter of the TEM_{00} cavity mode (74 μm) calculated by ABCD propagation matrix theory. A two-plane Gires-Tournois interferometer (GTI) mirror was used to compensate the intracavity group delay dispersion (GDD), which provided a total GDD of $\approx -800\ \mathrm{fs}^2$ per round. We used a plane OC with a transmittance of 1% for the spectral range of 1000–1100 nm.

APPENDIX B: THE FITTING PARAMETERS OBTAINED FROM Z-SCAN CHARACTERIZATION

As shown in Table 3, it summarizes the fitting parameters obtained from Z-scan characterization of InAsP NWs at the wavelength of 532 and 1064 nm, which shows the strong saturable absorption properties of InAsP NWs.

Table 3. Fitting Parameters Obtained from Z-Scan Characterization of InAsP NWs under Different Excitation Energies

Wavelength (nm)	Input Energy (μJ)	β_{eff} (cm/MW)	$\mathrm{Im}\chi^{(3)}$ ($\times 10^{-7}$ esu)	I_s (GW/cm^2)	ΔR	n_2 ($\times 10^{-13}$ m^2/W)	$\mathrm{Re}\chi^{(3)}$ ($\times 10^{-7}$ esu)
532	0.25	−207.4 ± 2.3	−2.63 ± 0.03	0.8 ± 0.02	0.337 ± 0.002	2.39 ± 0.03	7.17 ± 0.01
	0.16	−205.4 ± 1.7	−2.6 ± 0.02	0.81 ± 0.04	0.322 ± 0.002	2.46 ± 0.02	7.38 ± 0.01
	0.055	−203.4 ± 2.8	−2.59 ± 0.04	0.78 ± 0.05	0.324 ± 0.002	2.44 ± 0.03	7.32 ± 0.01
1064	1.01	−144 ± 0.7	−3.7 ± 0.02	0.25 ± 0.008	0.192 ± 0.002	2.73 ± 0.02	8.2 ± 0.01
	0.55	−146 ± 0.9	−3.7 ± 0.03	0.24 ± 0.006	0.148 ± 0.002	2.75 ± 0.03	8.3 ± 0.01
	0.33	−142 ± 1.1	−3.6 ± 0.03	0.24 ± 0.006	0.105 ± 0.002	2.76 ± 0.02	8.3 ± 0.01

APPENDIX C: THE NONLINEAR TRANSMITTANCE CURVE OF InAsP NWS

As shown in Fig. 5, the curve of the nonlinear transmittance with respect to the intensity of incident light was obtained by extracting the experimental data of the open-aperture (OA) Z-scan. The basic parameters of the InAsP NWs, which are summarized in Table 3, including saturation intensity and modulation depth, can be fitted using the following formula [37]:

$$T(Z) = 1 - \frac{\Delta R}{1 + \frac{I}{I_s}} - A_{\mathrm{ns}}, \tag{C1}$$

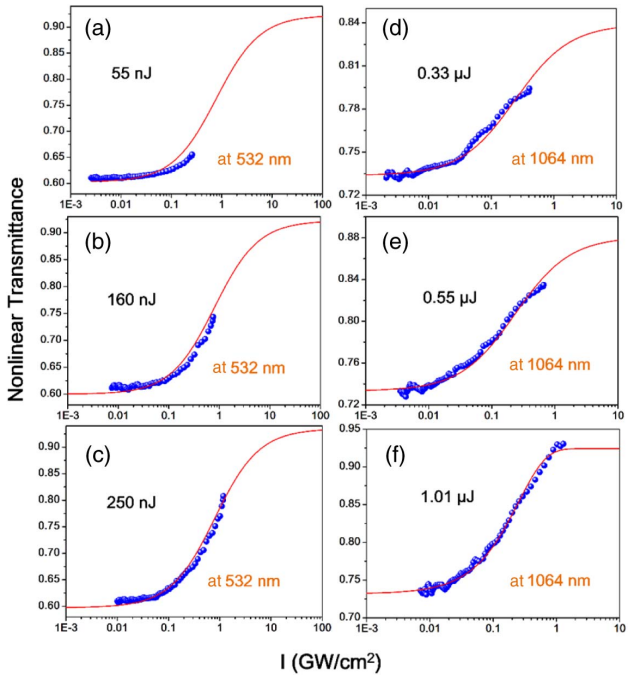

Fig. 5. (a)–(c) Nonlinear transmittance of the InAsP NWs at the wavelength of 532 nm with different incident pulse energies. (d)–(f) Nonlinear transmittance of the InAsP NWs at the wavelength of 1064 nm with different incident pulse energies.

where ΔR, I_s, and A_{ns} are modulation depth, saturable intensity, and nonsaturable loss, respectively.

APPENDIX D: THE EXPERIMENTAL SETUP OF THE MODE-LOCKED SOLID-STATE LASER

In our experiment, a z-type resonator with the cavity length of 3.49 m is applied, as shown in Fig. 6.

Funding. National Natural Science Foundation of China (61975095, 61975097); Qilu Young Scholar of Shandong University; Youth Cross Innovation Group of Shandong University (2020QNQT); Self-made Equipment Cultivation Project of Shandong University (ZY202002); European Union (H2020-MSCA-RISE-872049 (IPN-Bio)); Aalto University Doctoral School; Walter Ahlströmin Säätiö; Elektroniikkainsinöörien Säätiö; Sähköinsinööriliiton Säätiö; Nokia Foundation; Academy of Finland (320167).

Acknowledgment. H.Y. acknowledges the support from EU. V.K. acknowledges the support of Aalto University Doctoral School, Walter Ahlström Foundation, Elektroniikkainsinöörien Säätiö, Sähköinsinööriliiton Säätiö, and Nokia Foundation Finnish Foundation for Technology Promotion (Tekniikan Edistämissäätiö) and Waldemar Von Frenckells foundation. H.L. and V.K. acknowledge support from the Academy of Finland Flagship Programme, Photonics Research and Innovation (PREIN), decision number: 320167. V.K. and H.Y. acknowledge the provision of facilities and technical support by Aalto University at Micronova Nanofabrication Centre.

Disclosures. The authors declare no conflicts of interest.

REFERENCES

1. J. Wallentin, N. Anttu, D. Asoli, M. Huffman, I. Åberg, M. H. Magnusson, G. Siefer, P. Fuss-Kailuweit, F. Dimroth, B. Witzigmann, H. Q. Xu, L. Samuelson, K. Deppert, and M. T. Borgström, "InP nanowire array solar cells achieving 13.8% efficiency by exceeding the ray optics limit," Science **339**, 1057–1060 (2013).
2. H. Zhu, Y. Fu, F. Meng, X. Wu, Z. Gong, Q. Ding, M. V. Gustafsson, M. T. Trinh, S. Jin, and X. Y. Zhu, "Lead halide perovskite nanowire lasers with low lasing thresholds and high quality factors," Nat. Mater. **14**, 636–642 (2015).
3. H. Pettersson, J. Trägårdh, A. I. Persson, L. Landin, D. Hessman, and L. Samuelson, "Infrared photodetectors in heterostructure nanowires," Nano Lett. **6**, 229–232 (2006).

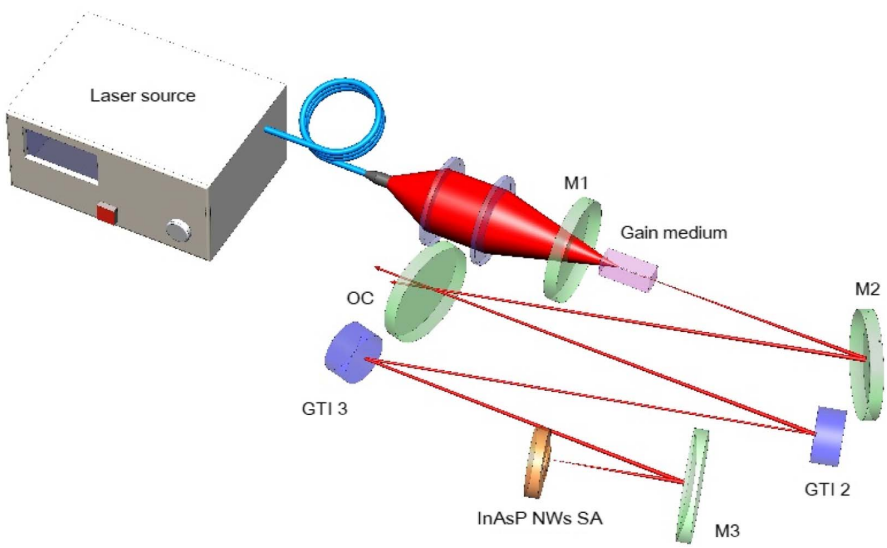

Fig. 6. Experimental setup of the mode-locked solid-state bulk laser based on an InAsP NWs SA.

4. N. Engheta, "Circuits with light at nanoscales: optical nanocircuits inspired by metamaterials," Science **317**, 1698–1702 (2007).
5. Y. S. No, L. Xu, M. N. Mankin, and H. G. Park, "Shape-controlled assembly of nanowires for photonic elements," ACS Photon. **3**, 2285–2290 (2016).
6. J. Kim, H. C. Lee, K. H. Kim, M. S. Hwang, J. S. Park, J. M. Lee, J. P. So, J. H. Choi, S. H. Kwon, C. J. Barrelet, and H. G. Park, "Photon-triggered nanowire transistors," Nat. Nanotechnol. **12**, 963–968 (2017).
7. Y. Cui and C. M. Lieber, "Functional nanoscale electronic devices assembled using silicon nanowire building blocks," Science **291**, 851–853 (2001).
8. D. M. Lyons, K. M. Ryan, M. A. Morris, and J. D. Holmes, "Tailoring the optical properties of silicon nanowire arrays through strain," Nano Lett. **2**, 811–816 (2002).
9. L. B. Luo, F. X. Liang, X. L. Huang, T. X. Yan, J. G. Hu, Y. Q. Yu, C. Y. Wu, L. Wang, Z. F. Zhu, Q. Li, and J. S. Jie, "Tailoring the electrical properties of tellurium nanowires via surface charge transfer doping," J. Nanopart. Res. **14**, 967–976 (2012).
10. S. M. Bergin, Y. H. Chen, and B. J. Wiley, "The effect of nanowire length and diameter on the properties of transparent, conducting nanowire films," Nanoscale **4**, 1996–2004 (2012).
11. V. Mourik, K. Zuo, S. M. Frolov, S. R. Plissard, E. Bakkers, and L. P. Kouwenhoven, "Signatures of majorana fermions in hybrid superconductor-semiconductor nanowire devices," Science **336**, 1003–1007 (2012).
12. L. Balaghi, G. Bussone, J. Grenzer, M. Ghorbani, A. Krasheninnikov, and H. Schneider, "Widely tunable GaAs bandgap via strain engineering in core/shell nanowires with large lattice mismatch," Nat. Commun. **10**, 2793 (2019).
13. M. Li and J. C. Li, "Size effects on the band-gap of semiconductor compounds," Mater. Lett. **60**, 2526–2529 (2006).
14. I. Åberg, G. Vescovi, D. Asoli, U. Naseem, J. P. Gilboy, C. Sundvall, A. Dahlgren, K. E. Svensson, N. Anttu, M. T. Björk, and L. Samuelson, "A GaAs nanowire array solar cell with 15.3% efficiency," IEEE J. Photovolt. **6**, 185–190 (2016).
15. Z. Liu, L. Yin, H. Ning, Z. Yang, L. Tong, and C. Z. Ning, "Dynamical color-controllable lasing with extremely wide tuning range from red to green in a single alloy nanowire using nanoscale manipulation," Nano Lett. **13**, 4945–4950 (2013).
16. M. D. Thompson, A. Alhodaib, A. P. Craig, A. Robson, A. Aziz, A. Krier, J. Svensson, L. E. Wernersson, A. M. Sanchez, and A. R. Marshall, "Low leakage-current InAsSb nanowire photodetectors on silicon," Nano Lett. **16**, 182–187 (2016).
17. A. L. Efros and M. Rosen, "The electronic structure of semiconductor nanocrystals," Annu. Rev. Mater. Res. **30**, 475–521 (2000).
18. S. K. Lim, M. Brewster, F. Qian, Y. Li, C. M. Lieber, and S. Gradečak, "Direct correlation between structural and optical properties of III–V nitride nanowire heterostructures with nanoscale resolution," Nano Lett. **9**, 3940–3944 (2009).
19. J. Hou, B. Zhang, X. Su, R. Zhao, Z. Wang, F. Lou, and J. He, "High efficient mode-locked Tm:YAP laser emitting at 1938 nm by SESAM," Opt. Commun. **347**, 88–91 (2015).
20. J. H. Lee, M. W. Pin, S. J. Choi, M. H. Jo, J. C. Shin, S. G. Hong, S. M. Lee, B. Cho, S. J. Ahn, N. W. Song, S. H. Yi, and Y. H. Kim, "Electromechanical properties and spontaneous response of the current in InAsP nanowires," Nano Lett. **16**, 6738–6745 (2016).
21. E. Lind, A. I. Persson, L. Samuelson, and L. E. Wernersson, "Improved subthreshold slope in an InAs nanowire heterostructure field-effect transistor," Nano Lett. **6**, 1842–1846 (2006).
22. M. Takiguchi, N. Takemura, K. Tateno, K. Nozaki, S. Sasaki, S. Sergent, E. Kuramochi, T. Wasawo, A. Yokoo, A. Shinya, and M. Notomi, "All-optical InAsP/InP nanowire switches integrated in a Si photonic crystal," ACS Photon. **7**, 1016–1021 (2020).
23. M. Karimi, M. Heurlin, S. Limpert, V. Jain, X. Zeng, I. Geijselaers, A. Nowzari, Y. Fu, L. Samuelson, H. Linke, M. T. Borgstrom, and H. Pettersson, "Intersubband quantum disc-in-nanowire photodetectors with normal-incidence response in the long-wavelength infrared," Nano Lett. **18**, 365–372 (2018).
24. J. Treu, M. Bormann, H. Schmeiduch, M. Doblinger, S. Morkotter, S. Matich, P. Wiecha, K. Saller, B. Mayer, M. Bichler, M. C. Amann, J. J. Finley, G. Abstreiter, and G. Koblmuller, "Enhanced luminescence properties of InAs-InAsP core-shell nanowires," Nano Lett. **13**, 6070–6077 (2013).
25. Q. Hu, P. Li, B. Zhang, B. Liu, L. Wang, and X. Chen, "Passively *Q*-switched Yb-doped dual wavelength fiber laser based on a gold-nanocage saturable absorber," Appl. Opt. **57**, 8242–8248 (2018).
26. X. Han, K. Wang, H. Long, H. Hu, J. Chen, B. Wang, and P. Lu, "Highly sensitive detection of the lattice distortion in single bent ZnO nanowires by second-harmonic generation microscopy," ACS Photon. **3**, 1308–1314 (2016).
27. N. M. Jassim, K. Wang, X. Han, H. Long, B. Wang, and P. Lu, "Plasmon assisted enhanced second-harmonic generation in single hybrid Au/ZnS nanowires," Opt. Mater. **64**, 257–261 (2017).
28. R. Carles, N. Saint-Cricq, J. B. Renucci, and R. J. Nicholas, "Raman scattering in $InP_{1-x}As_x$ alloys," J. Phys. C **13**, 899–910 (1980).
29. J. Guo, R. Shi, R. Wang, Y. Wang, F. Zhang, C. Wang, H. Chen, C. Ma, Z. Wang, Y. Ge, Y. Song, Z. Luo, D. Fan, X. Jiang, J. Xu, and H. Zhang, "Graphdiyne-polymer nanocomposite as a broadband and robust saturable absorber for ultrafast photonics," Laser Photon. Rev. **14**, 1900367 (2020).
30. M. Breusing, C. Ropers, and T. Elsaesser, "Ultrafast carrier dynamics in graphite," Phys. Rev. Lett. **102**, 086809 (2009).
31. H. Wang, C. Zhang, and F. Rana, "Surface recombination limited lifetimes of photoexcited carriers in few-layer transition metal dichalcogenide MoS_2," Nano Lett. **15**, 8204–8210 (2015).
32. D. Sun, Y. Rao, G. A. Reider, G. Chen, Y. You, L. Brezin, A. R. Harutyunyan, and T. F. Heinz, "Observation of rapid exciton-exciton annihilation in monolayer molybdenum disulfide," Nano Lett. **14**, 5625–5629 (2014).
33. J. S. Manser and P. V. Kamat, "Band filling with free charge carriers in organometal halide perovskites," Nat. Photonics **8**, 737–743 (2014).
34. M. Ghanassi, M. C. Schanne-Klein, F. Hache, A. I. Ekimov, D. Ricard, and C. Flytzanis, "Time-resolved measurements of carrier recombination in experimental semiconductor-doped glasses: confirmation of the role of Auger recombination," Appl. Phys. Lett. **62**, 78–80 (1993).
35. I. Robel, B. A. Bunker, P. V. Kamat, and M. Kuno, "Exciton recombination dynamics in CdSe nanowires: bimolecular to three-carrier Auger kinetics," Nano Lett. **6**, 1344–1349 (2006).
36. V. I. Klimov, A. A. Mikhailovsky, D. W. McBranch, C. A. Leatherdale, and M. G. Bawendi, "Quantization of multiparticle Auger rates in semiconductor quantum dots," Science **287**, 1011–1013 (2000).
37. J. Guo, D. Huang, Y. Zhang, H. Yao, Y. Wang, F. Zhang, R. Wang, Y. Ge, Y. Song, Z. Guo, F. Yang, J. Liu, C. Xing, T. Zhai, D. Fan, and H. Zhang, "2D GeP as a novel broadband nonlinear optical material for ultrafast photonics," Laser Photon. Rev. **13**, 1900123 (2019).
38. K. Wang, Y. Feng, C. Chang, J. Zhan, C. Wang, Q. Zhao, J. N. Coleman, L. Zhang, W. J. Blau, and J. Wang, "Broadband ultrafast nonlinear absorption and nonlinear refraction of layered molybdenum dichalcogenide semiconductors," Nanoscale **6**, 10530–10535 (2014).
39. S. Bikorimana, P. Lama, A. Walser, R. Dorsinville, S. Anghel, A. Mitioglu, A. Micu, and L. Kulyuk, "Nonlinear optical responses in two-dimensional transition metal dichalcogenide multilayer: WS_2, WSe_2, MoS_2 and $Mo_{0.5}W_{0.5}S_2$," Opt. Express **24**, 20685–20695 (2016).
40. K. Wang, B. M. Szydlowska, G. Wang, X. Zhang, J. J. Wang, J. J. Magan, L. Zhang, J. N. Coleman, J. Wang, and W. J. Blau, "Ultrafast nonlinear excitation dynamics of black phosphorus nanosheets from visible to mid-infrared," ACS Nano **10**, 6923–6932 (2016).
41. X. Jiang, S. Liu, W. Liang, S. Luo, Z. He, Y. Ge, H. Wang, R. Cao, F. Zhang, Q. Wen, J. Li, Q. Bao, D. Fan, and H. Zhang, "Broadband nonlinear photonics in few-layer MXene $Ti_3C_2T_x$ (T = F, O, or OH)," Laser Photon. Rev. **12**, 1700229 (2018).
42. J. Liu, V. Khayrudinov, H. Yang, Y. Sun, B. Matveev, M. Remennyi, K. Yang, T. Haggren, H. Lipsanen, F. Wang, B. Zhang, and J. He, "InAs-nanowire-based broadband ultrafast optical switch," J. Phys. Chem. Lett. **10**, 4429–4436 (2019).
43. M. Sheik-Bahae, A. A. Said, T. Wei, D. J. Hagan, and E. W. V. Stryland, "Sensitive measurement of optical nonlinearities using a single beam," IEEE J. Quantum Electron. **26**, 760–769 (1990).